ISSN 1063-7737, Astronomy Letters, 2020, Vol. 46, No. 1, pp. 1–11. © Pleiades Publishing, Inc., 2020.
Russian Text © The Author(s), 2020, published in Pis'ma v Astronomicheskii Zhurnal, 2020, Vol. 46, No. 1, pp. 3–14.

Redshift Measurements for Galaxies in Clusters by Multislit Spectroscopy at the 1.5-m Telescope RTT150

I. M. Khamitov[1,2*], I. F. Bikmaev[2,3], R. A. Burenin[4], M. V. Glushkov[2,3], S. S. Melnikov[2,3], and A. R. Lyapin[4]

[1] *TÜBİTAK National Observatory, Antalya, Turkey*

[2] *Kazan Federal University, ul. Kremlevskaya 18, Kazan, 420000 Russia*

[3] *Academy of Sciences of Tatarstan, ul. Baumana, 20, Kazan, Russia*

[4] *Space Research Institute, ul. Profsoyuznaya 84/32, Moscow, 117997 Russia*

Received December 4, 2019; revised December 4, 2019; accepted December 5, 2019

Abstract—An example of simultaneous spectroscopic redshift measurements for a large number of galaxies in a cluster by multiobject spectroscopy with the medium- and low-resolution TFOSC spectrograph at the Russian–Turkish 1.5-m telescope (RTT150) is presented. The redshifts of galaxies in the cluster 0301.6 + 0156 at $z = 0.17057 \pm 0.0004$ detected previously by the Sunyaev–Zeldovich signal in the Planck all-sky survey have been measured. The spectra of 16 cluster galaxies, 9 of which were determined as ellipticals, were taken in one observation with an exposure time of 3 h and high-quality redshift measurements were made for them. We show that the redshifts of galaxies with magnitudes to $m_r = 20.0$, whose number in the TFOSC field can reach dozens, depending on the cluster richness and distance, can be measured in one observation with the TFOSC spectrograph using multiobject masks. Such measurements may be required to refine the redshifts of clusters and to estimate their masses by the dynamical method.

DOI: 10.1134/S106377372001003X

Keywords: *galaxy clusters, multiobject spectroscopy, optical observations.*

INTRODUCTION

Galaxy clusters occupy an important place in studying the large-scale structure of the Universe. The observed number of galaxy clusters of a specific mass turns out to be very sensitive to cosmological model parameters, such as the mean matter mass in the Universe and the density perturbation amplitude (see, e.g., Vikhlinin et al. 2014). Therefore, galaxy clusters are a powerful tool in cosmological research that provides one of the principal means of measuring the cosmological parameters (see, e.g., Borgani et al. 2001; Vikhlinin et al. 2003, 2009; Mantz et al. 2010; Rozo et al. 2010; Pierre et al. 2011; Burenin and Vikhlinin 2012; Planck Collaboration 2014b, 2016c).

A large amount of work is carried out at the Russian–Turkish 1.5-m telescope (RTT150) on the optical identification and redshift measurement of rich galaxy clusters in large surveys, such as the ROSAT 400 square degree X-ray survey (Burenin et al. 2007) and the survey of galaxy clusters detected by the Sunyaev–Zeldovich signal (Sunyaev and Zeldovich 1972) with the Planck Space Observatory (Planck Collaboration 2014a, 2015a, 2015b, 2016a, 2016b; Vorobyev et al. 2016; Burenin 2017; Burenin et al. 2018; Zaznobin et al. 2019).

Spectroscopic redshift measurements for identified galaxy clusters are carried out at RTT150 mainly for systems at redshifts $z < 0.4$. The redshifts are estimated through spectroscopic observations of several brightest members at the cluster center or by observing only one brightest galaxy at the cluster center with a regular shape. This approach is determined by the efficiency of using the observing time of middle-class telescopes with mirror diameters of 1–2 m for such objects. The accuracy of redshift measurements achieved in this way ($\delta z \sim 0.001$) for the galaxy clusters being studied is sufficient for their use in research on constraining the cosmological parameters.

Since the brightest galaxy is virtually at the cluster center of mass, the measured redshift corresponds to the cluster redshift. Fainter galaxies are used only to confirm the red sequence on the color–luminosity diagram, based on which a preliminary identification of the cluster and its members is carried out. However, if the individual radial velocities of the galax-

*E-mail: irek_khamitov@hotmail.com

ies with respect to the brightest galaxy are taken into account, then the characteristic features in the spectra of elliptical cluster galaxies can be used to increase the efficiency and accuracy of determining the system redshift. By separating the red-sequence elliptical galaxies from the total set of galaxies, we can construct a composite spectrum with a better signal-to-noise ratio, i.e., collect the cluster photons from a larger area. Thus, a more accurate cluster redshift estimate can be obtained while using the telescope time much more efficiently.

In addition, the velocity dispersion of cluster members can be estimated during simultaneous spectroscopic observations of a large number of cluster galaxies by multislit spectroscopy. Such measurements are required both to estimate the total gravitational masses of individual clusters and to calibrate the scale of galaxy cluster masses when measured by other methods (see, e.g., Saro et al. 2013; Old et al. 2014; Ho et al. 2019).

In this paper we describe the technique of multi-object spectroscopic observations that can be carried out with the medium- and low-resolution TFOSC spectrograph at the 1.5-m Russian–Turkish telescope (RTT150). We provide a methodological description of the choice of apertures to construct the cluster mask, describe the spectrophotometric reduction of the spectra for the multislit data set, and measure the redshifts and velocity dispersions of galaxies using the observation of the galaxy cluster 0301.6 + 0156 from the extended Planck galaxy cluster catalogue (Burenin 2017) as an example.

GALAXY SELECTION AND MASK CONSTRUCTION

An efficient technique of simultaneous spectroscopic observations for a large number of extragalactic objects with multiobject spectrographs (MOS) has been developed in the last few decades. For example, these include ground-based instruments, such as the OSIRIS 10-m GTC telescope (Jordi 1998) or the SCORPIO 6-m BTA telescope (Afanasiev and Moiseev 2005), and the MOS being prepared for the launch of the 6.5-m James Webb Space Telescope with a controlled microshutter array based on MEMS technology (Jhabvala et al. 2008).

The bulk of the galaxies in a cluster are concentrated in a region up to 1 Mpc with their maximum near 0.5 Mpc (Capasso et al. 2019). Thus, at $z > 0.17$ the maximum number of cluster members are concentrated at distances less than 3 arcmin from the brightest cluster galaxy (BCG). The technique of spectroscopic observations of galaxy clusters with MOS is most efficient in terms of the expenditure of telescope time. The image scale in the RTT150 focal plane at the Cassegrain focus (F/7.7) is $17.8''$/mm (Aslan et al. 2001). Thus, it is possible to use only short slits in a stationary mask in investigating galaxy clusters by the MOS method at RTT150.

Indeed, setting up an optical-fiber collector of light simultaneously from a large number of sources is physically unfeasible due to the geometric sizes of the optical-fiber heads. The slit size across the spectrograph dispersion also limits the number of sources for spectroscopy. Clearly, the maximum number of simultaneously observed objects with nonoverlapping dispersion curves is reached in the case where the vertical and horizontal slit sizes coincide, i.e., when either a square or circular aperture is used.

In our observations we made a mask with circular apertures. The aperture size in the mask (200 μm) installed in the RTT150 focal plane corresponds to $3.5''$ in the field of view of the TFOSC light detector. The candidates were selected by the red sequence within $2'$ of the brightest cluster galaxy in such a way that the $r'-i'$ color was less than 0.05 of the linear fit and that the brightest galaxies fell into the mask, where possible.

The mask apertures were determined according to the following algorithm. The mask center is chosen to be the CCD detector image center and corresponds to the position of the brightest galaxy in the cluster 0301.6 + 0156 thus, the first aperture is chosen. The remaining apertures are determined as follows.

1. All of the galaxies differing from the BCG in $r'-i'$ color by no more than 0.05^m and located at angular distances within $1'$ in declination and $3'$ in right ascension from it and with a magnitude no fainter than 21^m in the r' band are selected using the photometric SDSS DR12 catalogue (Alam et al. 2015).

2. All of the sources lying within 1.5 aperture radii in right ascension from the BCG are excluded from the selected sample. Thus, all of the sources whose spectrum could partially overlap the BCG spectrum were excluded.

3. The brightest galaxy was chosen from the remaining list and its position determined the next aperture position.

4. All of the sources lying within 1.5 aperture radii in right ascension with respect to the source chosen in step 3 were excluded from the list.

5. Steps 3 and 4 are performed until the entire sample is exhausted.

6. At least two reference stars of an early spectral type, where possible, are chosen in the galaxy cluster field in order that the stellar spectrum be smooth, without features, in the region of strong telluric absorption lines. The spectra of these stars are used as reference ones to sum the spectra of the objects obtained at different epochs of observations and to take into account the telluric absorption lines.

7. Since the light from both the source and the sky background falls into a circular aperture, we face the problem of taking into account the level of the latter. It is solved by the addition of apertures in sky regions without bright sources within a radius of 10 arcsec located at the same positions in right ascension as the selected sources to the list of selected sources. The total image of the SDSS field in the $g'r'i'$ bands was used to select the sky apertures. First, all of the regions lying in a strip of 3 aperture radii in right ascension with respect to the selected sources were excluded from the image. The strip centers correspond to the positions of these sources. Then, all of the regions with a radius of $5''$ around all of the identified field sources at 3 standard deviations of the sky background were determined and masked. The positions of the sky background apertures least distant from the selected source were chosen from the remaining unmasked image.

8. A table of aperture positions in micrometers is constructed using the scale factor between the angular measure in the TFOSC field of view and the linear measure in the RTT150 focal plane. The scale factor determined from observations is 54.3 μm/arcsec.

9. A file in the .dxf format of the computer-aided design system with a specified template of the mask suitable for installation in the aperture wheel of the TFOSC system is created using the table of apertures.

In Fig. 1 the circles indicate the source apertures selected by the algorithm described above and the corresponding additional apertures to take into account the sky background of the cluster 0301.6 + 0156.

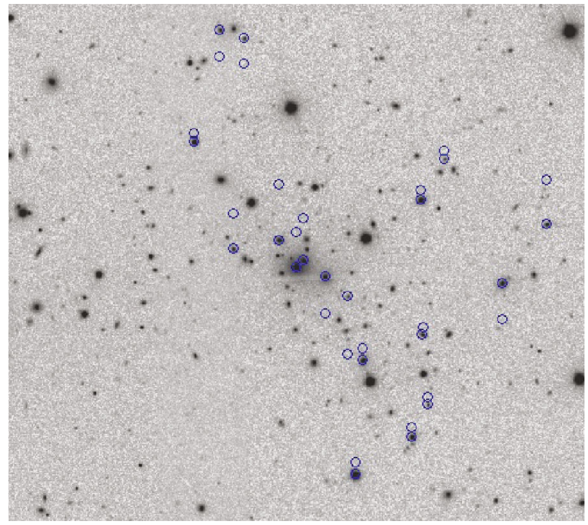

Fig. 1. (Color online) Image of cl0301.6 + 0156 in the TFOSC field of view. North (N) is leftward, east (E) is upward. The blue circles indicate the selected sources for the MOS mask construction and the corresponding additional apertures to take into account the sky background.

OBSERVATIONS AND MOS DATA REDUCTION

The observations of the cluster 0301.6 + 0156 with a mask of 18 sources (16 candidates for cluster members and two field stars: one as a reference star and the other as a comparison star) were carried out on November 13, 2018. Six spectral frames were taken with an exposure time of 1800 s each at airmasses from 1.3 to 2.4. The last frame was excluded from our analysis due to a weakly accumulated signal and a strong deviation of the atmospheric absorption from Bouguer's law at airmasses more than 2. We took the spectra of a Fe—Ar lamp with a line emission spectrum for the dispersion calibration and the spectra of a halogen lamp to take into account the interference fringes in the long-wavelength part of the spectra and to find the positions of the dispersion curves. All of the spectral frames, both from the sources and the calibration ones, were bias-corrected and the dark frames scaled to the frame exposure time were subtracted from them.

Extraction of the spectra. The procedure of searching for the positions and extracting the spectra was carried out according to the following algorithm:

1. The spectrum of a halogen lamp is recorded with the mask and the dispersive element (Fig. 2c).

2. A strip with a width of 10 pixels and a height equal to the full image length across the dispersion direction was selected in the central zone of the image. The profile that is a vertical cut of the recorded spectra is constructed from the median values at a given strip height (Fig. 3).

3. The positions of the local maxima are determined on the profile.

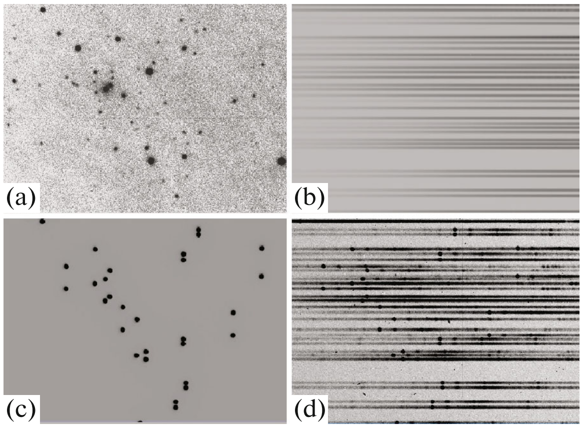

Fig. 2. (a) Field of cl0301.6 + 0156. (b) The field image through the mask. (c) The spectrum of a halogen lamp taken with the mask and grism 15. (d) The cluster spectrum taken with the mask and grism 15.

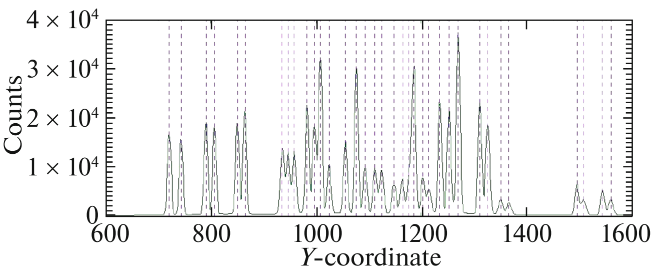

Fig. 3. Profile across the dispersion to determine the positions of the spectra.

4. The interval with the center at the largest maximum is fitted by a Gaussian. The center is written in the list of positions of the dispersion curves and the constructed fit is subtracted from the profile to reduce the influence of the wings on the adjacent maxima when determining an accurate position. The full width at half maximum (FWHM) of the Gaussian is also saved.

5. The largest local maximum is chosen from the remaining ones on the profile and procedure 4 is repeated until all of the dispersion positions on the vertical cut from the list are refined (Fig. 3).

6. Procedures 2–5 are then performed for the zones in the direction of decrease and and increase along the vertical axis relative to the central position with a step of 100 pixels each.

7. The central dispersion position (Y_c) for a given aperture in coordinate Y is well described by a quadratic polynomial of coordinate X.

8. The value of $\mathrm{FWHM_{avg}}$ averaged over all the FWHM values determined in procedure 4 is found.

9. The flux $F(X, Y_c)$ at a given coordinate X and central position Y_c for each dispersion curve, which is determined from the polynomial fit in procedure 7, was determined as the total flux of the image $\mathrm{Im}(X, Y)$ in the vertical interval $[Y_1, Y_2]$ weighted over Gaussian G with $\mathrm{FWHM_{avg}}$ and centered at Y_c:

$$F(X, Y_c) = \frac{\sum_{Y_1}^{Y_2}(\mathrm{Im}(X, Y_i) G_i W_i(X, Y_i))}{\sum_{Y_1}^{Y_2}(G_i W_i(X, Y_i))},$$

where Y_1 and Y_2 are integer values of the expressions $Y - \mathrm{FWHM_{avg}}$ and $Y + \mathrm{FWHM_{avg}}$, respectively. Such weighting is appropriate for reducing the influence of the wings of strong telluric lines on the adjacent spectra when observing faint objects with dispersion curves shifted relative to one another. The shift takes place, because the light from different apertures falls on the dispersive element at different angles. To take into account the fact that the real interval within which the flux is summed falls on a fractional pixel, we introduced a function $W(Y_i)$ defined as follows:

$$W(Y) = \begin{cases} 1, & \text{if } Y_1 < Y_i < Y_2 \\ 1 - \{Y - \mathrm{FWHM_{avg}}\}, & \text{if } Y_i = Y_1 \\ \{Y + \mathrm{FWHM_{avg}}\}, & \text{if } Y_i = Y_2, \end{cases}$$

where the expression in braces { } is the fractional part of the number.

DISPERSION CALIBRATION

Depending on the mask pinhole position in the detector field of view, the visible spectra are recorded in various spectral ranges. Figure 2b corresponds to the pinhole positions, while Fig. 2d displays the spectra of celestial sources corresponding to these pinholes. A strong telluric neutral oxygen emission line (5577.2 Å, [O I]) is clearly identified in each spectrum. This line is clearly seen to be shifted, depending on the pinhole position. As has already been noted above, this shift takes place, because the light from different apertures falls on the dispersive element at different angles.

Based on the spectra of a Fe–Ar calibration lamp taken using the mask with pinholes and grism 15 of the TFOSC system and the NOAO web resource,[1]

[1] http://iraf.noao.edu/specatlas/fear/fear.html.

Table 1. Determination of the emission line coordinate ($X_{\rm line}$) in the Fe–Ar calibration spectrum taken with grism 15 of the TFOSC system from the linear dependence on pinhole X coordinate $X_{\rm pinhole}$: $X_{\rm line} = a_0 + a_1 X_{\rm pinhole}$

Line	Wavelength (Å)	a_0	a_1
Ar I	4158.6	−697.8	1.00649
Ar II	4481.8	−559.3	1.00451
Ar II	4545.1	−530.4	1.00308
Ar II	4657.6	−481.2	1.00090
Ar II	4764.9	−436.1	1.00031
Ar II	4806.0	−418.7	0.99989
Ar II	4879.9	−387.3	0.99967
Ar II	4965.1	−352.2	0.99902
Ar II	5062.0	−312.0	0.99823
Fe I	5269.5	−226.1	0.99707
Fe I	5328.0	−201.5	0.99693
Ar I	5495.9	−131.7	0.99528
Ar I	6032.1	87.1	0.99072
Ar II	6114.9	117.1	0.99062
Fe I	6172.3	141.6	0.99009
Ar II	6416.3	240.0	0.98782
Ar I	6677.3	343.0	0.98733
Ar I	6871.3	421.7	0.98395
Ar I	6965.4	459.0	0.98305
Ar I	7067.2	499.5	0.98197
Ar I	7147.0	531.3	0.98100
Ar I	7272.9	580.8	0.98005
Ar I	7384.0	624.4	0.97933
Ar I	7635.1	723.5	0.97673
Ar I	7948.2	846.0	0.97393
Ar I	8264.5	969.5	0.97071
Ar I	8521.4	1069.1	0.96849
Ar I	8667.9	1126.0	0.96694

we measured the positions of some of the brightest and barely blended iron and argon lines for the spectra of the corresponding pinhole. It turned out that, to a first approximation, the lamp line positions are described with an accuracy of 1–2 pixels by a linear dependence on pinhole coordinate X. This allowed a code for automatic dispersion calibration of spectra to be written, which we used subsequently. Table 1 gives the identifications of the Fe–Ar lamp lines used by us, their wavelengths, and the corresponding coefficients of the linear dependence on pinhole coordinate X.

More accurate line positions are calculated using directly the Fe–Ar spectra. To determine the exact maximum of the corresponding line, we used a parabolic fit within ±4 pixels around the approximate value in pinhole X coordinate precalculated from the coefficients of the linear dependence from Table 1. For all spectra the dispersion solution is described by a cubic polynomial; the rms deviation was less than 2 Å.

CORRECTION FOR INTERFERENCE ON THE CCD STRUCTURE

In the DW436N-BV Andor CCD detector used by us interference is observed on the CCD structure in the red spectral range at wavelengths longer than 7000 Å. The variations of the recorded signal due to interference complicate significantly the reduction of the spectra in the near-infrared range of electromagnetic radiation. To take into account the influence of interference, we used a standard approach based on the spectrum of a halogen lamp ($S_{\rm hal}$). The spectrum of a halogen lamp obtained for a given pinhole was smoothed by a moving average with a 30-pixel window, which was fitted by a fifth-degree polynomial (P_5) in the range of wavelengths longer than 7000 Å. The spectrum distortion due to interference ($K_{\rm fringe}$) is defined as the ratio of the fit and the spectrum of a halogen lamp:

$$K_{\rm fringe} = \frac{P_5}{S_{\rm hal}}.$$

Subsequently, all spectra for a given aperture were corrected by simple multiplication by $K_{\rm fringe}$. Figures 4 and 5 show the instrumental spectrum of the comparison star and the result of correcting the interference pattern in the red region of the same spectrum, respectively. We see a significant reduction of the flux variations in the stellar spectrum in this spectral region.

CORRECTION FOR THE SKY BACKGROUND

In contrast to long-slit spectroscopic observations, in the spectra taken from small apertures the sky background cannot be directly taken into account by its estimation in the neighborhoods of a source. Therefore, we made additional pinholes in the mask located at the same positions along the dispersion as the sources, but shifted across the dispersion. There are also accuracy limitations in making identical (in size) pinholes. In addition, microscopic dust grains

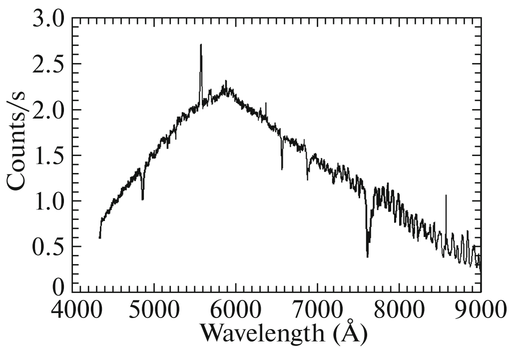

Fig. 4. Instrumental spectrum of the reference star.

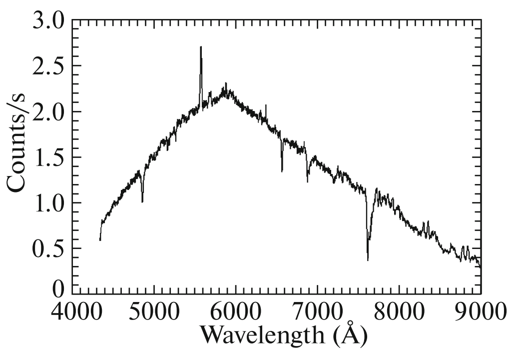

Fig. 5. Instrumental spectrum of the reference star after correction for interference.

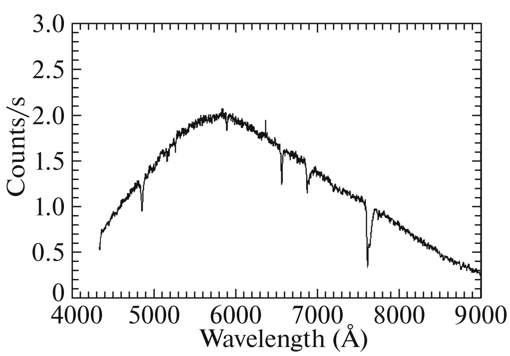

Fig. 6. Instrumental spectrum of the reference star after correction for the sky background.

may be present at the pinhole edges. These variations in the pinhole area lead to different recorded fluxes from the sky background, which poses the problem of scaling the recorded spectra.

Since the sky background uniformly fills the pinhole and the sources being investigated are sufficiently faint (at the sky background level or fainter), the total flux in a strong telluric neutral oxygen emission line (O I, 5577.2 Å) can be used to take into account the background flux variations due to the difference in pinhole area and to scale two different spectra. To estimate the O I line flux, the spectrum was fitted by a Gaussian and a linear wavelength dependence at distances less than 80 Å from the line center. The flux was taken as an integral of the Gaussian in the chosen region, while the terms of the linear dependence are a continuum estimate. All of the spectra from the additional pinholes were recalculated to integer wavelengths in angstroms and reduced to a single flux. As a reference spectrum for the flux scaling we chose the sky background spectrum with the greatest O I line flux. Then, we constructed a composite spectrum of the sky background as follows:

$$Sky(\lambda) = \begin{cases} F_1(\lambda), & \text{if } N = 1 \\ 0.5(F_1(\lambda) + F_2(\lambda)), & \text{if } N = 2 \\ \text{median}(F_{\overline{(1,N)}}(\lambda)), & \text{if } N > 2, \end{cases}$$

where λ runs all values from the shortest to the longest wavelength from all spectra with a 1 Å step; N is the total number of spectra at a given wavelength. Before its subtraction from the object spectrum, the composite sky background spectrum was scaled to the O I line flux of the object spectrum. Figure 6 shows the instrumental spectrum of the comparison after the sky background subtraction.

CORRECTION FOR THE TELLURIC H_2O, O_2, O_3 ABSORPTION LINES

In ground-based spectroscopic observations of celestial sources the spectra exhibit strong telluric absorption lines produced by molecules in the Earth's atmosphere. For high-altitude observatories, including the TUBITAK National Observatory where RTT150 is located, the main sources of absorption in telluric lines are water molecules (H_2O), molecular oxygen (O_2), and ozone (O_3). Whereas O_3 creates a broad, from 5000 to 7000 Å, smooth absorption line and reduces the flux of incoming radiation only by a few percent, the influence of O_2 and H_2O is more complex and pronounced. Figure 7 shows the wavelength dependences of the atmospheric transmission for O_3, O_2, and H_2O, respectively. We constructed the dependences based on the TAPAS web resource[2] (Bertaux et al. 2014) of the Pic du Midi Observatory at the time of our observations.

The wavelength dependences of the atmospheric transmission obtained with a high spectral resolution were convolved with a broadband Gaussian ($\sigma \sim$ 10 Å) characterizing the transfer function of the TFOSC system. Strong atmospheric absorption in the O_2 and H_2O lines above 6700 Å veils the spectral features of elliptical cluster galaxies falling on these lines. When determining the redshifts of

[2] http://cds-espri.ipsl.fr/tapas/.

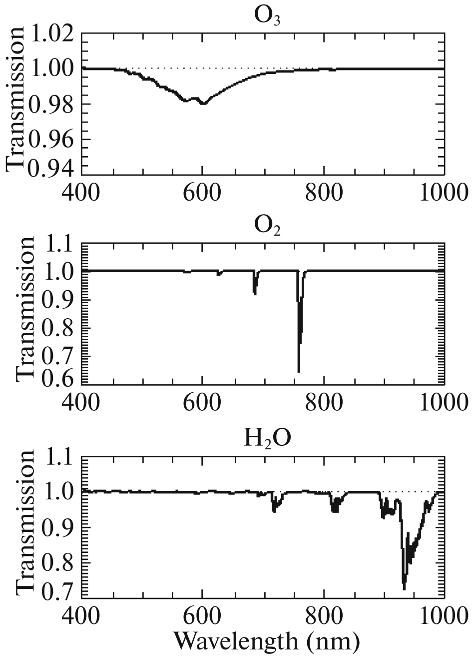

Fig. 7. Atmospheric transmission in the telluric O_3, O_2, and H_2O lines.

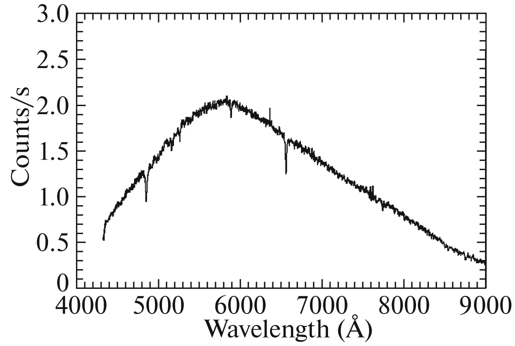

Fig. 8. Instrumental spectrum of the reference star after correction for the telluric absorption lines.

these light sources by the cross-correlation method with a template spectrum, the exclusion of prominent features, such as the G, Mg, and NaD absorption lines and the jump near 4000 Å, make the estimates somewhat noisy. In the spectra of main-sequence stars of spectral type F or earlier there are no distinct features in the region of the atmospheric transparency windows and the telluric lines themselves from 7000 to 9000 Å. Since these lines are relatively narrow, the change in CCD detector sensitivity and the influence of the telescope and spectrograph optics may can assumed to be linear. Consequently, the continuum in this spectral region can be constructed with confidence, while the deviations from it will be due to the atmospheric absorption alone. Thus, the atmospheric transmission in the H_2O and O_2 lines can be obtained by comparing the spectra of F-type stars and the dependence constructed based on TAPAS.

In simultaneous observations of a large number of sources all spectra are recorded under identical atmospheric conditions. Therefore, the presence of a star of an appropriate spectral type among the sources allows the spectral distribution of all the sources being investigated to be reconstructed before the radiation enters the Earth's atmosphere in the region of the telluric H_2O and O_2 lines. We used the condition $g-r < 0.34$, corresponding to a main-sequence star earlier than F9 V, when choosing a comparison star. The telluric O_3 line is fairly broad. Therefore, the continuum in this region is difficult to determine, because the assumption about a linear dependence of the instrumental sensitivity is incorrect. However, since the line is formed in the Earth's upper atmospheric layers, without a great loss of accuracy we can adopt this dependence as that for the Pic du Midi Observatory. Figure 8 shows the instrumental spectrum of the reference star after removing the contribution from the telluric absorption lines.

COMPOSITE SPECTRUM CONSTRUCTION

Long signal accumulation is required in observations of faint sources and, consequently, the recorded spectra will correspond to different atmospheric conditions. The presence of a reference star among the sources allows the instrumental sensitivity and atmospheric transparency correction coefficients to be found even if the observations were not carried out under spectrophotometric conditions. This requires the spectral distribution of the reference star in energy units that is obtained by a standard method with the long-slit observation of a spectrophotometric standard under favorable atmospheric conditions. Assuming that the flux from the reference star does not change in the time of our observations, we can then process the spectra corrected for the atmosphere and instrumental sensitivity and obtain a composite spectrum with a better signal-to-noise ratio.

Even if the observations were carried out on different nights, the flux from the reference star can be controlled photometrically using additional observations in broadband filters. The spectrophotometric standard HR718 [3] was used for the spectrophotometric calibration of the reference star. To obtain the composite spectrum, we used the median values of five spectra taken at airmasses less than 2. Figures 9–11 present the composite spectra of the reference star, the comparison star, and the BCG.

[3] https://www.eso.org/sci/observing/tools/standards-/spectra/hr718.html.

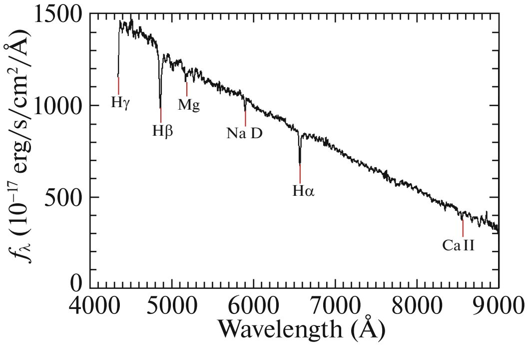

Fig. 9. (Color online) Composite spectrum of the reference star.

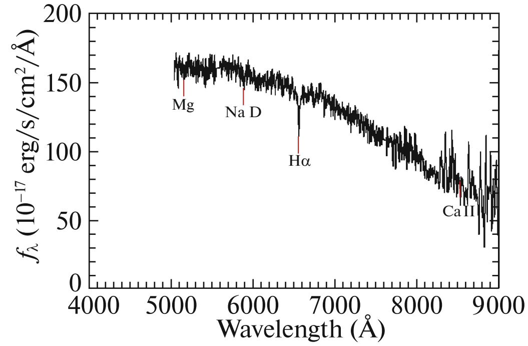

Fig. 10. (Color online) Composite spectrum of the comparison star.

The spectrum of the reference star corresponds to a giant of spectral type F. A distinct Balmer absorption series, a Ca II triplet, and a Mg absorption line are observed. Judging by the spectrum, the stellar temperature derived from Gaia DR2 data ($T_{\rm eff} = 5112$ K, $d = 500$ pc) was determined erroneously. At the distance of the reference star interstellar extinction contributes significantly to the NaD absorption line; it is $A_V = 0.243$ toward the cluster (Schlegel et al. 1998).

The spectra of the comparison star show a variable pattern; the continuum flux changes approximately by a factor of $\sim$1.5 in the time of our observations $\sim$3 h. We also recorded a shift in the Hα line; the source approaches with a velocity $\sim$300 km s^{-1}. The Gaia parallax gives an estimate $\sim$10 kpc with the same error. The large error may be related to the system binarity. On the other hand, at such a distance the comparison star would be fainter than the observed one by 2–3 magnitudes ($\sim 20\overset{m}{.}0$ for a G-type star). The question about the binarity of the comparison star remains open.

The BCG spectrum was taken with good accumulation and the main features, absorption lines, are clearly seen. It turned out that the NaD line falls almost exactly on the strong telluric O_2 line. It can be seen that, despite this fact, we were able to efficiently reconstruct it. The circle marks the narrow NaD absorption line formed by the Milky Way matter on the line of sight toward the BCG. Strong Hα and N II emission lines are also seen, pointing to star formation processes in the galaxy.

CLUSTER MEMBER GALAXY IDENTIFICATION, REDSHIFT AND VELOCITY DISPERSION MEASUREMENTS

Nine E-type galaxies were identified among the candidates for cluster members by a visual inspection. The redshift was measured by the same method as that used in our paper on measuring the redshifts of galaxy clusters from the Planck survey (Planck Collaboration 2015a; Vorobyev et al. 2016; Zaznobin et al. 2019) the cross-correlation method with a template spectrum. As a template we may take the spectrum of a nearby elliptical galaxy with a high signal-to-noise ratio or use the synthetic spectrum. The template spectrum is shifted relative to the galaxy spectrum with a certain step; in each step the χ^2 value is calculated as the square of the difference between the galaxy spectrum and the shifted template spectrum. Thus, the χ^2 value is determined as a function of the template spectrum shift. We find the sought-for shift and its measurement error by calculating the minimum of χ^2.

Table 2 gives our high-quality redshift measurements and the corresponding errors for these objects. An accuracy of our redshift determinations $\delta z/z \approx 0.001$ is achieved for elliptical galaxies with magnitudes to $19\overset{m}{.}5$ in the r band of the SDSS photometric system. Apart from the elliptical galaxies, we identified four objects as spiral galaxies and failed to identify two objects due to an insufficiently accumulated signal. One spectrum turned out to be noisy due to the sky lines from an adjacent pinhole because of the technological inaccuracy in the mask production. We see that the redshifts of galaxies with magnitudes to $m_r = 20.0$ can be measured in one observation with the TFOSC spectrograph using multiobject masks.

Based on our redshift measurements, we estimated the velocity dispersion of the cluster being investigated to be $\sigma_v = 530 \pm 60$ km s^{-1}. Our estimate of the BCG redshift that we take as the cluster redshift is $z_{\rm BCG} = 0.16987 \pm 0.0005$. The cluster redshift can be refined from multiobject data. This requires summing all spectra of elliptical cluster galaxies, i.e., collecting the photons from a larger area, thereby increasing the signal-to-noise ratio of the composite spectrum. As a result, we construct the weighted mean (in brightness) spectrum for a large number of galaxies with the averaging of their radial velocities. A more accurate z measurement for the cluster, which,

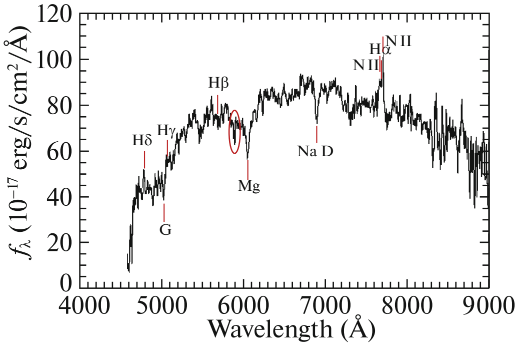

Fig. 11. (Color online) Composite BCG spectrum.

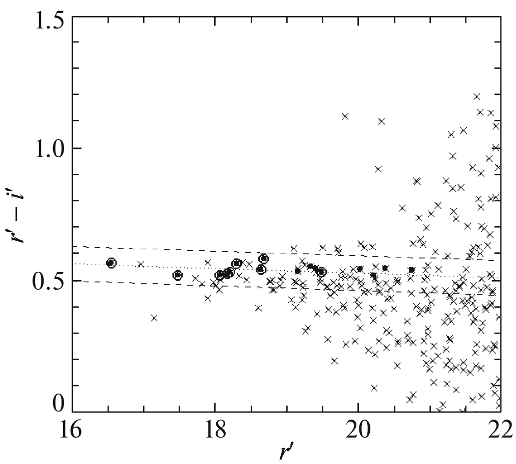

Fig. 12. Red sequence in the region of cl0301.6 + 0156 and spectroscopically identified elliptical cluster galaxies (circles).

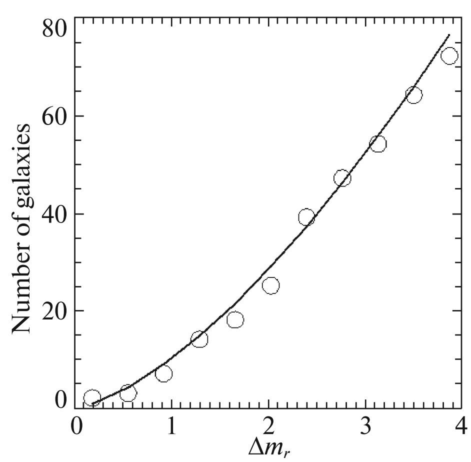

Fig. 13. Total number of galaxies determined from the red sequence in cl0301.6 + 0156 versus difference between a given magnitude and the BCG magnitude.

as expected, was found with a better accuracy, is obtained from this spectrum, $z_{cl} = 0.17057 \pm 0.0004$.

RED-SEQUENCE REFINEMENT AND THE POTENTIAL NUMBER OF CANDIDATES

Based on the identified cluster members, we can also refine the red sequence. For our cluster it is described by the expression

$$r' - i' = 0.704 - 0.009r'.$$

The measured rms deviation of the galaxy positions from the red sequence is $0\overset{m}{.}02$ in $r'-i'$. Figure 12 shows the color $(r'-i')$—magnitude (r') diagram for all galaxies to 22^m within $3'$ of the BCG. The circles mark the galaxies that entered into the list of sources for which the spectra were taken. The bigger circles mark the identified E-type cluster galaxies. The dashed lines mark the zones at a distance of 3 standard deviations from the central line of the red sequence. By restricting ourselves to $m_r \leq 21.0$, we counted to the total number of galaxies as a function of the difference between a given magnitude and the BCG magnitude. This dependence is well fitted by an exponential function with an exponent close to 3/2. Figure 13 shows the result of fitting the total number of galaxies lying within 3σ inside the red sequence by the function $N_{\rm gal} = 10\Delta m_r^{\frac{3}{2}}$. The potential number of candidates in the mask in the TFOSC field of view can be estimated using this dependence.

The optimal distance between the pinholes along an axis perpendicular to the dispersion direction to obtain nonoverlapping spectra is $6''$. Thus, up to 100–110 spectra can potentially be obtained in a $11'$ field of view; the pinhole corresponding to the object need not be made to estimate the sky background. It will suffice to uniformly determine ten apertures over the entire field and to construct a composite spectrum of the sky background from them, as was determined in this paper in the section "Correction for the Sky Background." On the other hand, the galaxy cluster is a compact structure that is limited, on average, by 1 Mpc in size and the galaxies in the projection visible to us are distributed in both coordinates. Consequently, the total number of galaxies in one mask will be half the total number or a significant fraction of candidates can be covered by two masks. Beginning from $z < 0.1$, the angular size of 1 Mpc is more than $10'$ and the entire CCD field can be used. The total number of galaxies in this case is $\sim$100 candidates. For clusters at $z > 0.3$ the angular cluster size decreases to 2 arcmin and the total number of galaxies below the established limit for RTT150 ($m_r \leq 20.0$) is 30 candidates. Thus, it can be concluded that in the case of massive galaxy clusters at redshifts $z < 0.3$, it is possible to carry out highly accurate redshift measurements for 15 to 50 galaxies based on the RTT150 observations performed with only one mask.

Table 2. Results of our redshift measurements of the candidates for members of cl0301.6 + 0156. The photometric redshift measurements of the objects ($z_{\rm phot}$) were taken from the SDSS DR12 catalogue

RA(J2000)	DEC(J2000)	r	$g-r$	$r-i$	$z_{\rm phot}$	z	$z_{\rm err}$	Note
03 01 31.20	+01 56 26.1	18.65	1.29	0.54	0.214	0.17026	0.0008	
03 01 34.36	+01 55 55.7	18.31	1.29	0.56	0.197	0.17591	0.0006	
03 01 37.54	+01 57 21.9	18.17	1.21	0.52	0.182	0.16543	0.0009	
03 01 37.80	+01 55 32.3	18.08	1.29	0.52	0.212	0.16523	0.0006	
03 01 38.20	+01 55 14.6	16.55	1.31	0.56	0.175	0.16987	0.0005	BCG
03 01 38.48	+01 55 18.9	17.49	1.26	0.52	0.176	0.16902	0.0005	
03 01 38.96	+01 54 35.5	19.50	1.34	0.53	0.233	0.17309	0.0008	
03 01 39.33	+01 55 04.0	18.69	1.25	0.58	0.195	0.16918	0.0006	
03 01 40.98	+01 56 31.6	18.21	1.34	0.53	0.192	0.17004	0.0006	
03 01 32.52	+01 56 36.0	20.39	0.97	0.55	0.298			Faint
03 01 35.43	+01 56 32.6	19.41	1.23	0.55	0.222			S-type
03 01 36.99	+01 55 46.4	20.23	1.33	0.52	0.257			S-type
03 01 39.97	+01 57 49.4	19.16	1.25	0.53	0.202			Bad pinhole position
03 01 42.67	+01 56 46.3	20.76	1.09	0.54	0.362			Faint
03 01 47.67	+01 54 42.3	20.04	1.36	0.54	0.241			S-type
03 01 48.01	+01 54 27.4	19.34	1.34	0.55	0.247			S-type
RA(J2000)	DEC(J2000)	r	$g-r$	$r-i$	Star			
03 01 29.62	+01 55 51.0	15.31	0.32	0.11	Reference			
03 01 43.38	+01 54 11.4	17.09	0.33	0.15	Comparison			

CONCLUSIONS

We presented an example of simultaneous spectroscopic redshift measurements for a large number of galaxies in a cluster by multiobject spectroscopy. The redshifts of galaxies in the cluster 0301.6 + 0156 at $z = 0.17057 \pm 0.0004$ detected previously by the Sunyaev–Zeldovich signal in the Planck all-sky survey (Burenin 2017) were measured.

The spectra of 16 cluster galaxies, 9 of which were determined as ellipticals, were taken in one observation with an exposure time of 3 h with the medium- and low-resolution TFOSC spectrograph at the 1.5-m Russian–Turkish telescope (RTT150) using multiobject field masks and high-quality redshift measurements were made for them. Four more galaxies were determined as spirals, two objects could not be identified due to an insufficiently accumulated signal, and one spectrum was noisy due to the sky lines from an adjacent pinhole.

We showed that the redshifts of galaxies with magnitudes to $m_r = 20.0$ could be measured in one observation with the TFOSC spectrograph using multiobject masks. In a $\sim 11' \times 11'$ field, depending on the cluster richness and distance, the total number of simultaneous spectroscopic measurements for galaxies can be from 15 to 50 for clusters at $z < 0.3$. Such measurements may be required in future to refine the redshifts of clusters and to estimate their masses by the dynamical method.

ACKNOWLEDGMENTS

We thank TÜBİTAK, the Space Research Institute, the Kazan Federal University, and the Academy of Sciences of Tatarstan for their partial support in using RTT150 (the 1.5-m Russian–Turkish telescope in Antalya).

FUNDING

This work was supported by RSF grant no. 18-22-00520. The work of S. Melnikov was partially funded by the subsidy 3.67 14.2017/8.9 allocated to the Kazan Federal University for the State assignment in the sphere of scientific activities.

REFERENCES

1. P. A. R. Ade, N. Aghanim, C. Armitage-Caplan, et al. (Planck 2013 Results XXIX), Astron. Astrophys. **571**, A29 (2014a); arXiv:1303.5089.
2. P. A. R. Ade, N. Aghanim, C. Armitage-Caplan, et al. (Planck 2013 Results XX), Astron. Astrophys. **571**, A20 (2014b).
3. P. A. R. Ade, N. Aghanim, M. Arnaud et al. (Planck Intemediate Results XXVI), Astron. Astrophys. **582**, A29 (2015a); arXiv:1407.6663.
4. P. A. R. Ade, N. Aghanim, C. Armitage-Caplan, et al. (Planck 2013 Results XXXII), Astron. Astrophys. **581**, A14 (2015b); arXiv:1502.00543.
5. P. A. R. Ade, N. Aghanim, M. Arnaud, et al. (Planck Intermediate Results XXXVI), Astron. Astrophys. **586**, A139 (2016a); arXiv:1504.04583.
6. P. A. R. Ade, N. Aghanim, M. Arnaud, et al. (Planck 2015 Results XXVII), Astron. Astrophys. **594**, A27 (2016b); arXiv:1502.01598.
7. P. A. R. Ade, N. Aghanim, M. Arnaud, et al. (Planck 2015 Results XXIV), Astron. Astrophys. **594**, A24 (2016c); arXiv:1502.01597.
8. V. L. Afanasiev and A. V. Moiseev, Astron. Lett. **31**, 194 (2005).
9. S. Alam, F. D. Albareti, C. A. Prieto, F. Anders, S. F. Anderson, T. Anderton, B. H. Andrews, E. Armengaud, et al., Astrophys. J. Suppl. Ser. **219**, 12 (2015).
10. Z. Aslan, I. F. Bikmaev, E. A. Vitrichenko, R. I. Gumerov, L. A. Dembo, S. F. Kamus, V. Keskin, U. Kiziloglu, et al., Astron. Lett. **27**, 398 (2001).
11. J. L. Bertaux, R. Lallement, S. Ferron, C. Boonne, and R. Bodichon, et al., Astron. Astrophys. **564**, A46 (2014).
12. S. Borgani, P. Rosati, P. Tozzi, S. A. Stanford, P. R. Eisenhardt, C. Lidman, B. Holden, R. D. Ceca, et al., Astrophys. J. **561**, 13 (2001).
13. R. A. Burenin, Astron. Lett. **43**, 507 (2017).
14. R. A. Burenin and A. A. Vikhlinin, Astron. Lett. **38**, 347 (2012).
15. R. A. Burenin, A. Vikhlinin, A. Hornstrup, H. Ebeling, H. Quintana, and A. Mescheryakov, Astrophys. J. Suppl. Ser. **172**, 561 (2007).
16. R. A. Burenin, I. F. Bikmaev, I. M. Khamitov, I. A. Zaznobin, G. A. Khorunzhev, M. V. Eselevich, V. L. Afanasiev, S. N. Dodonov, J.-A. Rubiño-Martín, N. Aghanim, and R. A. Sunyaev, Astron. Lett. **44**, 297 (2018).
17. R. Capasso, J. J. Mohr, A. Saro, A. Biviano, N. Clerc, A. Finoguenov, S. Grandis, C. Collins, et al., Mon. Not. R. Astron. Soc. **486**, 1594 (2019).
18. M. Ho, M. M. Rau, M. Ntampaka, A. Farahi, H. Trac, B. Póczos, et al., Astrophys. J. (2019, in press); arXiv:1902.05950.
19. M. D. Jhabvala, D. Franz, T. King, G. Kletetschka, A. S. Kutyrev, M. J. Li, S. E. Meyer, S. Moseley, et al., Proc. SPIE **6959**, 17 (2008).
20. C. Jordi, Astrophys. Space Sci. **263**, 369 (1998).
21. A. Mantz, S. W. Allen, D. Rapetti, and H. Ebeling, Mon. Not. R. Astron. Soc. **406**, 1759 (2010).
22. L. Old, R. A. Skibba, F. R. Pearce, D. Croton, S. I. Muldrew, J. C. Muñoz-Cuartas, D. Gifford, M. E. Gray, et al., Mon. Not. R. Astron. Soc. **441**, 1513 (2014).
23. M. Pierre, F. Pacaud, J. B. Juin, J. B. Melin, P. Valageas, N. Clerc, P. S. Corasaniti, et al., Mon. Not. R. Astron. Soc. **414**, 1732 (2011).
24. E. Rozo, R. H. Wechsler, E. S. Rykoff, J. T. Annis, M. R. Becker, A. E. Evrard, J. A. Frieman, S. M. Hansen, et al., Astrophys. J. **708**, 645 (2010).
25. A. Saro, J. J. Moh, G. Bazin, and K. Dolag, Astrophys. J. **772**, 17 (2013).
26. D. J. Schlegel, D. P. Finkbeiner, M. Davis, Astrophys. J. **500**, 525 (1998).
27. R. A. Sunyaev and Ya. B. Zeldovich, Comm. Astrophys. Space. Phys. **4**, 173 (1972).
28. A. Vikhlinin, A. Voevodkin, C. R. Mullis, L. van Speybroeck, H. Quintana, B. R. McNamara, I. Gioia, A. Hornstrup, et al., Astrophys. J. **590**, 15 (2003).
29. A. Vikhlinin, A. V. Kravtsov, R. A. Burenin, H. Ebeling, W. R. Forman, A. Hornstrup, C. Jones, S. S. Murray, et al., Astrophys. J. **692**, 1060 (2009).
30. A. A. Vikhlinin, A. V. Kravtsov, M. L. Markevich, R. A. Syunyaev, and E. M. Churazov, Phys. Usp. **57**, 317 (2014).
31. V. S. Vorob'ev, R. A. Burenin, I. F. Bikmaev, I. M. Khamitov, S. N. Dodonov, R. Ya. Zhuchkov, et al., Astron. Lett. **42**, 63 (2016).
32. I. A. Zaznobin, R. A. Burenin, I. F. Bikmaev, I. M. Khamitov, G. A. Khorunzhev, V. V. Konoplev, M. V. Eselevich, V. L. Afanasiev, S. N. Dodonov, J.-A. Rubiño-Martín, N. Aghanim, and R. A. Sunyaev, Astron. Lett. **45**, 492 (2019).

Translated by V. Astakhov